Journal of Solid State Chemistry **155,** 320–325 (2000)
doi:10.1006/jssc.2000.8920, available online at http://www.idealibrary.com on IDEAL®

Mechanical Alloying and Thermal Decomposition of $(ZrO_2)_{0.8}$–$(\alpha\text{-}Fe_2O_3)_{0.2}$ Powder for Gas Sensing Applications

W. Cao, O. K. Tan,[1] W. Zhu, and B. Jiang

Sensors & Actuators Lab, Microelectronics Centre, School of EEE, Nanyang Technological University, 50 Nanyang Avenue, Singapore 639798

Received May 1, 2000; in revised form July 21, 2000; accepted August 9, 2000; published online November 29, 2000

The mechanical alloying process of $(ZrO_2)_{0.8}$–$(\alpha\text{-}Fe_2O_3)_{0.2}$ powder during high-energy ball milling at room temperature and the thermal decomposition of $(ZrO_2)_{0.8}$–$(\alpha\text{-}Fe_2O_3)_{0.2}$ powder at high temperature were studied by XRD, TEM, and differential thermal analysis. It was found that monoclinic zirconia transforms to cubic zirconia stabilized by Fe^{3+} after a milling time of 60 h. With the increased milling time up to 120 h, the powder appeared to consist of amorphous-like conglomerates. This metastable compound decomposed at a temperature of 650°C. The expulsion of the $\alpha\text{-}Fe_2O_3$ from the cubic ZrO_2 correlated directly with the current conductivity behavior and the oxygen gas sensing property of the thick film devices screen printed from this powder. The substitutional model $Fe_2O_3 \leftrightarrows 2Fe_{Zr}' + V_0^{\cdot\cdot} + 3O_0$ was adapted to explain both the mechanical alloying and thermal decomposition processes. © 2000 Academic Press

Key Words: **mechanical alloying; decomposition; nanocrystal; oxygen sensor.**

1. INTRODUCTION

Zirconium dioxide is technologically a very important material that can be used for practical applications not only as a structural ceramic but also as a functional material. One of the interesting applications of stabilized cubic ZrO_2 is oxygen gas sensing (1–4). Although the ZrO_2-based ceramic electrolyte oxygen gas sensor has been used commercially, the operating temperature of this type of sensor is very high, normally 700–900°C. Several attempts have been made to lower the operating temperature of zirconia-based oxygen sensors. However, none of these sensors has achieved sufficiently good oxygen sensing at low operating temperature. In our previous papers, a new kind of oxygen-sensitive and electrical-resistive material, ZrO_2 based with $\alpha\text{-}Fe_2O_3$ thick film oxygen gas sensor, has been investigated for low operating temperature (5, 6), and a preliminary gas sensing property has also been characterized (5). A gas sensitivity value of 166 to 20% oxygen has been obtained for optimal composition powder, $(ZrO_2)_{0.8}$–$(\alpha\text{-}Fe_2O_3)_{0.2}$, at a very low operating temperature of 325°C only. In this paper, we discuss the mechanical alloying process and the thermal decomposition process during the preparation of this stabilized zirconia.

At ambient pressure, pure zirconia possesses three crystallographic forms: monoclinic, tetragonal, and cubic. When the temperature changes, zirconia undergoes phase change; monoclinic/tetragonal transition at 1150°C and tetragonal/cubic transition at 2370°C (7–9). In order to obtain stabilized zirconia (s-ZrO_2) at room temperature, the high-energy ball milling method was employed to prepare nanosized cubic zirconia from the powder mixture of monoclinic zirconiza (m-ZrO_2) and a stabilizer, such as $\alpha\text{-}Fe_2O_3$. The substitution model of cubic ZrO_2 stabilized by Fe^{3+} expressed as $Fe_2O_3 \rightarrow 2Fe_{Zr}' + V_0^{\cdot\cdot} + 3O_0$ is well understood and widely accepted (8, 10–12). However, the stabilized powder synthesized from high-energy ball milling is stable only below a certain temperature, and it decomposes at high temperatures above 650°C. These observations explain the experimental results obtained for the thermal stability and gas sensing property of the $(ZrO_2)_{0.8}$–$(\alpha\text{-}Fe_2O_3)_{0.2}$ powder. A modified model, $Fe_2O_3 \rightleftarrows 2Fe_{Zr}' + V_{0\cdot\cdot} + 3O_{0'}$ was adapted to explain these phenomena.

2. EXPERIMENTAL PROCEDURE

For the preparation of the powder samples, powders of hematite, $\alpha\text{-}Fe_2O_3$, (99.9% purity; particle size, $< 5\ \mu m$), and zirconia, m-ZrO_2, (99% purity, 325 mesh), were mixed with a mole composition of $(ZrO_2)_{0.8}$–$(\alpha\text{-}Fe_2O_3)_{0.2}$. The mixing was carried out using the planetary ball mill (Fritsch Pulverisette 5). An open container with tungsten carbide (93 wt% WC and 6 wt% Co) vials and balls was chosen. The vial had a volume of 250 ml with an inner diameter of 75 mm and the balls had diameters of 10 and 20 mm. The milling speed was set at 200 rpm and the ball–to–powder weight ratio was 20 : 1. During milling air was constantly available to the oxide powder. Some amount of the milled

[1]To whom correspondence should be addressed. Fax: 065-7912687. E-mail: eoktan@ntu.edu.sg.

0022-4596/00 $35.00

powder was taken out of the vial for analysis and preparation of thick film paste at different milling times. The right number of balls was also taken out so as to maintain the 20 : 1 ball-to-powder weight ratio. The intervals were fixed at 2, 20, 60, and 120 h of milling.

The milled powder samples taken at different milling times were characterized using a Siemens D5005 X-ray diffractometer with Cu$K\alpha_1$ radiation at room temperature. The diffractometer range, 2θ, was from 20° to 60°. The scan speed was set at 1°/min. For thermal stability study, heat treatments for the 120-h milled $(ZrO_2)_{0.8}$–$(\alpha\text{-}Fe_2O_3)_{0.2}$ samples were carried out at 600, 700, and 800°C in air for 1 h. The X-ray diffraction (XRD) characterization was followed to investigate the effect of the heat treatments. The microstructures of the milled powders and heat-treated powders were studied using the Jeol JEM2010 transmission electron microscope (TEM) to observe the decomposition. TEM specimens were prepared by standard methods. The fine powders were scattered in ethanol by ultrasonic vibration, sprayed on to holey carbon films, and dried in air. Differential thermal analysis (DTA) was performed using a Perkin–Elmer differential thermal analyzer (DTA-7) for the milled $(ZrO_2)_{0.8}$–$(\alpha\text{-}Fe_2O_3)_{0.2}$ powder. The temperature range was from room temperature to 1000°C. The raising and lowering rate of the temperature was set at 4°C/min. The thick film screen printing process was employed to fabricate the oxygen gas sensor. The direct current conductivity and gas sensing properties were characterized using a Keithley 236 source measurement unit in the home-designed gas sensing measurement system (13). The carry gas was nitrogen and test gas was oxygen diluted in nitrogen.

3. RESULTS AND DISCUSSION

3.1. Mechanical Alloying Process

The $(ZrO_2)_{0.8}$–$(\alpha\text{-}Fe_2O_3)_{0.2}$ samples for different milling times were investigated by X-ray diffraction. Figure 1 shows the X-ray diffraction patterns of these milled powders. As a reference, the pattern of the unmilled $(ZrO_2)_{0.8}$–$(\alpha\text{-}Fe_2O_3)_{0.2}$ powder mixed thoroughly in an agate bowl is also attached. It presents the peaks of crystalline monoclinic ZrO_2 and corundum $\alpha\text{-}Fe_2O_3$. For samples with 2-h milling, these main peaks do not shift, but their intensities reduce due to the peaks' broadening. This indicates that the basic structure does not change yet, only the reduction of the grain size has occurred during the first 2 h of milling. This reduction of grain size is due to the impacts that occur in the vials between the balls and walls of the vials and the ball-to-ball collisions during the high-energy ball milling process. After a milling time of 20 h, the three main peaks of cubic ZrO_2 (111), (200), and (220), in 2θ range from 20° to 60°, can be observed. After a milling time of 60 h, the peaks of monoclinic ZrO_2 and corundum $\alpha\text{-}Fe_2O_3$ disappear

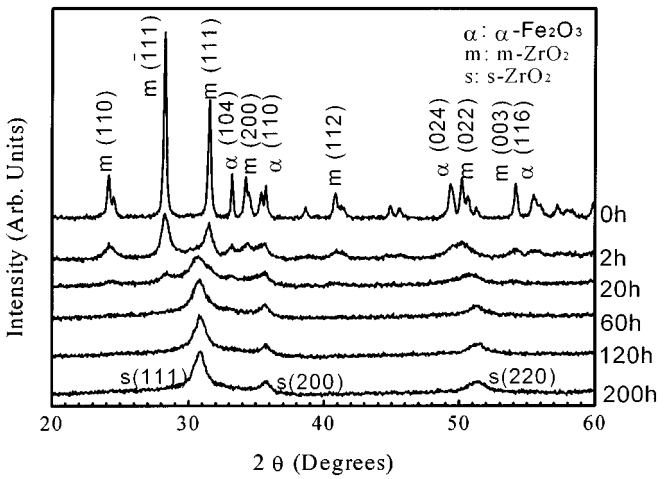

FIG. 1. X-ray diffraction patterns for samples milled for different times.

completely. There is no significant change in the XRD peaks with further milling. With prolonged milling, the impact energies derived are more than sufficient to kick the iron ions into the zirconia structure and transform the phase from monoclinic to cubic.

This alloying process was further investigated using TEM. Figures 2a and 2b show the morphology and selected area diffraction (SAD) pattern of the powders milled for 2 h and 120 h, respectively, as a typical observation. Figure 2c shows the dark-field image of the sample milled for 120 h. For particles milled for 2 h, most of the particle size was reduced down to about 25 nm. SAD clearly shows two sets of diffraction rings (Fig. 2a), which come from monoclinic ZrO_2 and corundum $\alpha\text{-}Fe_2O_3$, respectively. For particles milled for 120 h, no sign of individual particle from the bright-field image can be found in Fig. 2b, even at the thin edges of the sample. The dark-field image (Fig. 2c) shows that it is composed of small particles 8 nm in size. These particles are difficult to disperse by ultrasonic vibration in TEM specimen preparation. They always conglomerate together and formed a large lump. One postulation is that these nanoparticles are glued together in an amorphous-like matrix, that is, supported by the selected area electron diffraction (Fig. 2b). This SAD pattern gives a clear amorphous diffraction ring in addition to the diffraction rings of cubic ZrO_2. Hence, the powder milled after 120 h has an amorphous-like topology. Moreover, no diffraction point belonging to $\alpha\text{-}Fe_2O_3$ particles could be found. This dissolution of the Fe_2O_3 in the cubic ZrO_2 phase can be explained by the substitution model of $Fe_2O_3 \rightarrow 2Fe_{Zr}' + V_O^{\cdot\cdot} + 3O_O$ (8, 10–12).

The variation of particle size with the milling time was obtained by TEM observation. The results are depicted in Fig. 3. The average grain size of the particles reduces down to about 25 nm from 100 nm quickly during

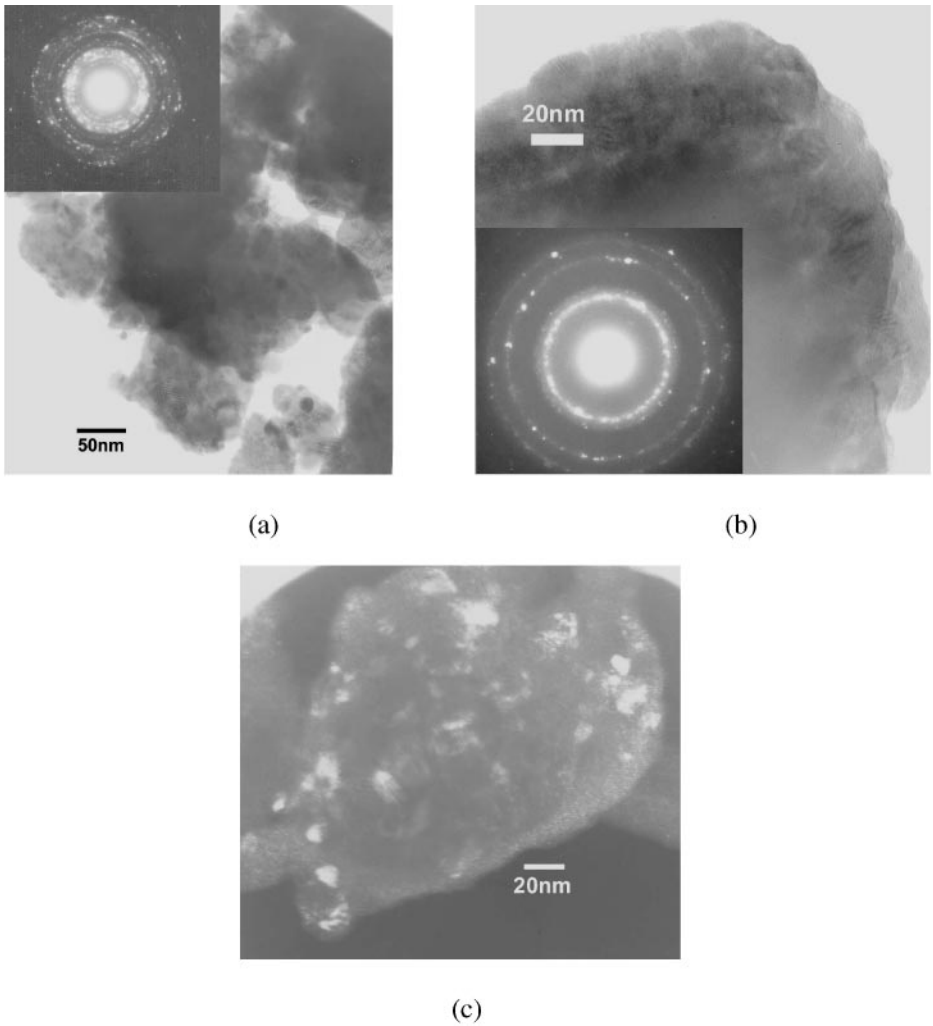

FIG. 2. TEM images for the $(ZrO_2)_{0.8}$–$(\alpha\text{-}Fe_2O_3)_{0.2}$ powder milled for different times. (a) TEM bright-field image and SAD pattern of the sample milled for 2 h. (b) TEM bright-field image and SAD pattern of the sample milled for 120 h. (c) TEM dark-field image of the sample milled for 120 h.

the first 2 h of milling. After which, the particle size reduces down to 8 nm more gradually with the milling time up to 120 h.

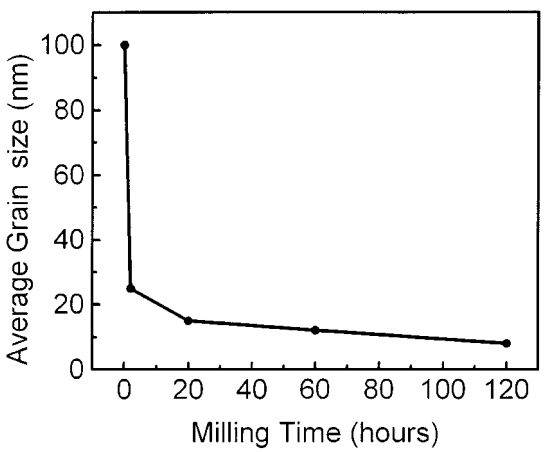

FIG. 3. Variation of the average grain size with the milling time.

3.2. *Thermal Decomposition Process*

Figure 4 depicts the DTA result for the $(ZrO_2)_{0.8}$–$(\alpha\text{-}Fe_2O_3)_{0.2}$ powder. There is an exothermic peak at 650°C while the temperature goes up. This implies a sudden phase change at 650°C during the increasing temperature cycle. However, there is no inverse transformation during the decreasing temperature cycle. In order to clarify this process, the $(ZrO_2)_{0.8}$–$(\alpha\text{-}Fe_2O_3)_{0.2}$ powder is heat-treated for 1 h in air at 600, 700, and 800°C, respectively. For the powder annealed at 600°C, its color remains yellowish-brown, just the same as that of the nonannealing powder. However, the color of the powder annealed at 700°C turns brown, further changes into reddish-brown when the powder is annealed at 800°C, indicating the possible structural change in these powder samples. Both TEM and XRD are therefore employed to investigate the phase change during this thermal process.

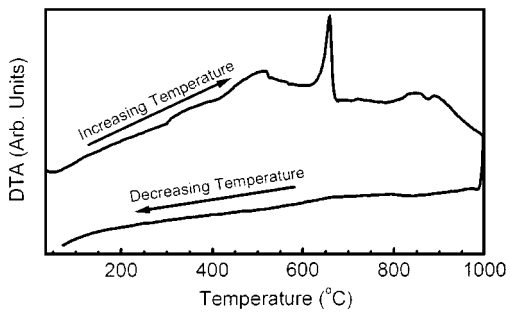

FIG. 4. Differential thermal analysis of the $(ZrO_2)_{0.8}$–$(\alpha\text{-}Fe_2O_3)_{0.2}$ powder at a heating rate of 4°C/min in air.

Figures 5a and 5b are SAD patterns of $(ZrO_2)_{0.8}$–$(\alpha\text{-}Fe_2O_3)_{0.2}$ powder samples annealed in air for 1 h at 600 and 700°C, respectively. In Fig. 5a, no diffraction rings or points of the $\alpha\text{-}Fe_2O_3$ phase can be found. Even the strongest diffraction (014) of $\alpha\text{-}Fe_2O_3$ located between the diffraction ring of (200) and (220) of s-ZrO_2 does not appear. On the contrary, for the sample annealed at 700°C, the (014) diffraction of the $\alpha\text{-}Fe_2O_3$ phase is clearly observed and marked in Fig. 5b. There is no essential difference between SAD images of the samples annealed at 700 and 800°C except the diffraction intensity. This TEM image observation indicates that the Fe^{3+} ions expel from the cubic ZrO_2 cell to form Fe_2O_3 constituent oxide when the sample undergoes annealing at a temperature between 600 and 700°C. Combined with the result of differential thermal analysis, the thermal decomposition is believed to start at around 650°C. This interesting thermal decomposition has not been previously observed and reported. In this light, the substitution model can be modified as $Fe_2O_3 \leftrightarrows 2Fe_{Zr}' + V_O^{\cdot\cdot} + 3O_O$ to account for the reverse decomposition process. This conclusion is also confirmed by the XRD characterization. Figure 6 shows the X-ray diffraction patterns of $(ZrO_2)_{0.8}$–$(\alpha\text{-}Fe_2O_3)_{0.2}$ samples annealed at 600, 700, and 800°C for 1 h. The X-ray diffraction pattern of the nonannealing sample is also shown. It can be seen that the peaks of the samples annealed at 600, 700, and 800°C are sharper and much more intense than those of the nonannealed one due to the reduction of surface defect and grain growth. A new peak corresponding to that of (014) of $\alpha\text{-}Fe_2O_3$ can be indexed in the 800°C annealed sample. The other peak (110) of $\alpha\text{-}Fe_2O_3$ overlaps with the peak (200) of cubic ZrO_2, and hence it is not observed. It is believed that this (014) peak is not observable at 700°C in XRD pattern because of its weak diffraction intensity, although it is seen in the SAD images because of its small quantity.

3.3. Electrical Conductivity and Gas Sensing Property

The behavior of the direct current conductivity of this material has been studied (6). Figure 7 depicts the conductivity of the thick film of $(ZrO_2)_{0.8}$–$(\alpha\text{-}Fe_2O_3)_{0.2}$ in air at different operating temperatures. The thick films were annealed for 1 h in air at different temperatures of 400, 500, 600, 700, and 800°C, respectively. For the samples annealed from 400 to 600°C, there are two distinct gradients from the plotted conductivity graph that indicate two regions of conduction and hence two activation energies. It was found that the transition from predominantly electronic to ionic conduction occurs at about 325°C. Above this transitional temperature, the conduction is contributed mainly by oxygen vacancies generated by the solid state reaction, and below this transitional temperature the conduction is dominated by electrons. This finding coincides with the result reported by Wilhelm *et al.* (10). For the samples annealed at

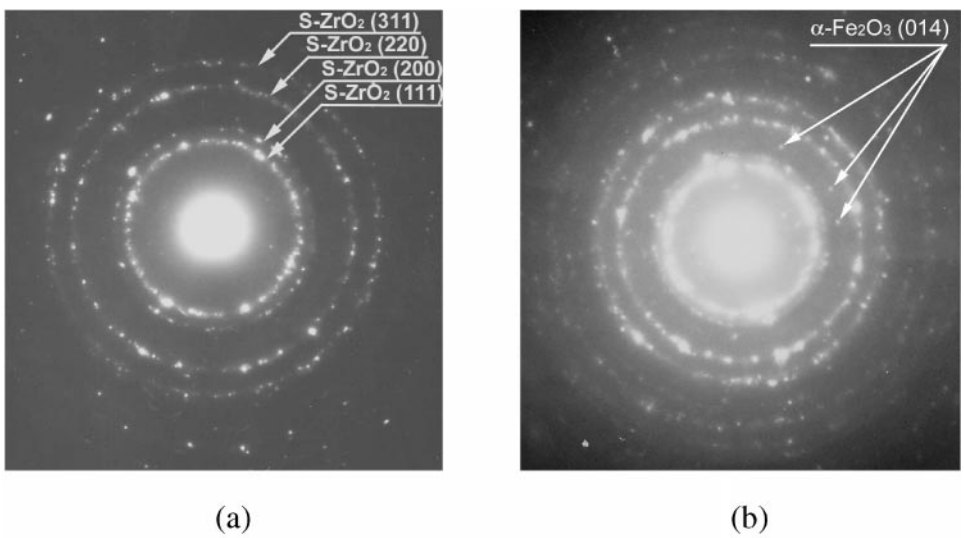

FIG. 5. SAD patterns for the $(ZrO_2)_{0.8}$–$(\alpha\text{-}Fe_2O_3)_{0.2}$ powder milled for 120 h and heat-treated at different temperatures. (a) 600°C, (b) 700°C.

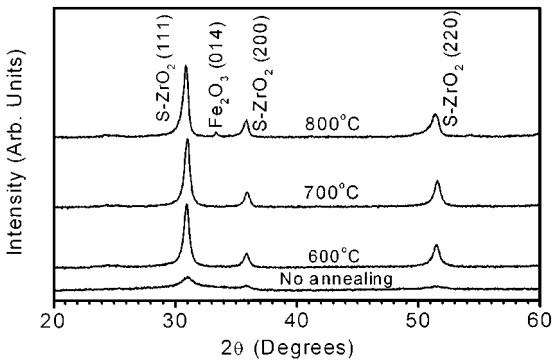

FIG. 6. X-ray diffraction patterns of the sample milled for 120 h and heat-treated at different temperatures.

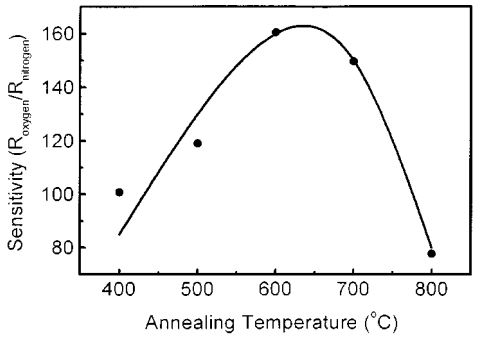

FIG. 8. Gas sensitivity to 20% oxygen operating at 325°C versus the annealing temperature.

700 and 800°C, the variation of the conductivity does not conform to this regularity anymore. The conductivity graph of sample annealed at 800°C shows only one single conduction region. Clearly, the conduction mechanism of samples changes when the annealing temperature raises from 600 to 800°C because of the expulsion of the Fe^{3+} from ZrO_2. The presence of the Fe_2O_3, which is semiconductor, increases the conductivity further.

As a potential low temperature oxygen gas sensor material, the gas sensing properties were investigated in our previous studies (5, 6). Figure 8 depicts the sensitivity of this material to 20% oxygen at the operating temperature of 325°C versus the annealing temperature. It is observed that the sensitivity increases with annealing temperature for the annealing temperature range lower than 650°C. However, it decreases with annealing temperature when the annealing temperature is higher than 650°C. It is believed that this inflection point is related to the onset of the expulsion of the Fe^{3+} ions and the conduction of the oxygen vacancies (14).

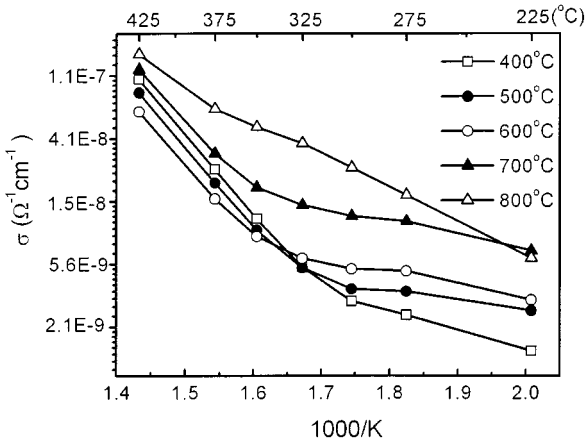

FIG. 7. Direct current electrical conductivity of $(ZrO_2)_{0.8}$–$(\alpha\text{-}Fe_2O_3)_{0.2}$ thick film in air for different annealing temperatures.

Below the annealing temperature of 650°C, the intrinsic oxygen vacancy concentration is as high as 18.5% in our 20 mol% Fe_2O_3 milled samples (8). This results in high conductivity and gas sensitivity. Beyond 650°C, the onset of the expulsion of iron ions results in a decrease in the oxygen vacancy concentration. With further increase in annealing temperature, the intrinsic oxygen vacancy concentration could be reduced drastically and hence its conductivity and gas sensitivity are also reduced.

4. CONCLUSION

Nano-sized powder has been prepared using the high-energy ball milling technique. As a result of mechanical alloying of 60 h, the monoclinic zirconia transforms to cubic zirconia stabilized by Fe^{3+}. With the increase of the milling time to 120 h, the powder becomes amorphous-like conglomerates. The particles with an average size of 8 nm can be observed in the TEM dark-field image. When this metastable cubic zirconia is subjected to heat treatment, Fe^{3+} ions expel as $\alpha\text{-}Fe_2O_3$ from the cubic ZrO_2 at 650°C. This thermal decomposition process correlates well with the behavior of the direct current conductivity and gas sensing property of the $(ZrO_2)_{0.8}$–$(\alpha\text{-}Fe_2O_3)_{0.2}$ material.

REFERENCES

1. A. D. Brailsford, M. Yussouff, and E. M. Logothetis, *Sens. Actuators B* **13–14,** 135 (1993).
2. A. D. Brailsford, M. Yussouff, E. M. Logothetis, and M. Shane, *Sens. Actuators B* **24–25,** 362 (1995).
3. S. Setnic, L. Rabco, and A. Diaconu, "CAS'97—Proceedings of 1997 International Semiconductor Conference, 7–11 Oct. 1997," p. 153.
4. M. Nakao, H. Sato, K. Kamimura, and Y. Onuma, "Proceedings of 1995 Japan International Electronic Manufacturing Technology Symposium, 4–6 December 1995," p. 162.
5. O. K. Tan, W. Zhu, W. Cao, and L. B. Kong, *in* "101st Annual Meeting & Exposition of the American Ceramic Society, Indianapolis, 25–28 April 1999," p. 166.

6. W. Cao, O. K. Tan, W. Zhu, P. E. Se Tho, and C. L. Yap, "Proceedings of 1st International Conference on Thermophysical Properties of Materials, 17–19 November 1999," p. 437.
7. A. M. Tonejc and A. Tonejc, *Mater. Sci. Forum* **225–227,** 497 (1996).
8. J. Z. Jiang, F. W. Poulsen, and S. Mϕrup, *J. Mater. Res.* **14,** 1343 (1999).
9. F. J. Berry, *J. Solid State Chemistry* **83,** 91 (1989).
10. R. V. Wilhelm, Jr., and D. S. Howarth, *Ceram. Bull.* **58,** 228 (1979).
11. G. Chiodelli, G. Flor, and M. Scagliotti, *Solid State Ionics* **91,** 109 (1996).
12. R. K. Sharma, M. C. Bhatnagar, and G. L. Sharma, *Sens. Actuators B* **45,** 209 (1997).
13. O. K. Tan, "Ferroelectric and Semiconductor Film Gas Sensors," Ph.D. thesis, Nanyang Technological University, 1998.
14. W. Cao, O. K. Tan, W. Zhu, and B. Jiang, submitted for publication.